Convection-Permitting Regional Climate Simulations Over Tibetan Plateau: Re-Initialization Versus Spectral Nudging

Mengnan Ma
Nanjing University https://orcid.org/0000-0003-4796-685X
Pinhong Hui
Jiangsu Provincial Meteorological Bureau
Dongqing Liu
Nanjing Meteorological Bureau
Peifeng Zhou
Nanjing University
Jianping Tang (jptang@nju.edu.cn)
Nanjing University

Research Article

Keywords: Tibet Plateau, spectral nudging, re-initialization, summer precipitation, surface air temperature, convection-permitting

Posted Date: June 1st, 2021

DOI: https://doi.org/10.21203/rs.3.rs-516962/v1

Version of Record: A version of this preprint was published at Climate Dynamics on October 9th, 2021.
See the published version at https://doi.org/10.1007/s00382-021-05988-2.

Abstract

Two regional climate simulation experiments (spectral nudging and re-initialization) at convection-permitting scale are conducted using the WRF model over the Tibetan Plateau (TP). The surface air temperature (T2m) and the precipitation in summer during 2016–2018 are evaluated against the in-situ station observations and the Global Satellite Mapping of Precipitation (GSMaP) dataset. The results show that both experiments can successfully capture the spatial distribution and the daily variation of T2m and precipitation, with reasonable cold bias for temperature, dry bias for precipitation when compared with the station observations. In addition, the diurnal cycle of precipitation is investigated, indicating that both experiments tend to simulate the afternoon precipitation in advance and postpone the night precipitation. The precipitation bias is reduced by using the spectral nudging technique, especially at night and early morning. Possible causes for the differences between the two experiments are also analyzed. The daytime surface net radiation contributes a lot to the cold biases in the re-initialization experiment, and the stronger low-level moisture flux convergence leads to the wet biases. These results can provide valuable guidance for further fine-scale simulation studies over the TP.

Key Points

1. Two regional climate simulation approaches (spectral nudging and re-initialization) at convection-permitting scale using WRF have comparable ability in reproducing the local climate characteristics in summer over TP
2. Cold bias is related to the daytime surface net radiation and wet bias is related to the stronger moisture flux convergence in the experiment with re-initialization scheme
3. Two WRF experiments successfully capture the bimodal structure of the diurnal variation of precipitation with reasonable wet bias

1. Introduction

The Tibet Plateau (TP), often known as the third pole of the Earth, is the largest and highest plateau in the world, with an average altitude of 3,000 to 5,000 meters and the maximum altitude above 8,000 meters (Kang et al. 2010). Due to its unique topography and geographical location, the TP exerts an important influence on regional weather and climate, even spreading to the whole Asia and all around the world through both thermal and mechanical forcing (Duan and Wu 2005; Yeh and Gao 1979). It has been called as ‘the driving force’ and ‘the amplifier’ for the global climate change (Pan et al. 1996). In addition, it is also the source of many Asian river systems and serves as ‘the Asian water tower’ (You et al. 2012). The regional climate change over the TP has an important impact on the regional hydrological cycle and even the river discharge of Asia (Su et al. 2013). More and more attention has been paid to the regional climate change over the TP, and it is very essential to obtain the detailed regional climate characteristics to accurately evaluate the sustainability of water resources and the impact of climate change over the TP.

Regional climate models (RCMs), which can well describe the regional characteristics such as local topography and land-use distribution, have been widely used to conduct the regional climate research and project the future climate change over the TP (Wang et al. 2013; Gao et al. 2015). Using the Weather Research and Forecasting (WRF) model driven by the global reanalysis dataset, Gao et al. (2015) conducted a 33-yr regional climate simulation over the TP with the resolution at 30km. The results presented that the RCM could improve the simulation of annual cycles of precipitation and surface air temperature in the wet season. Long-term regional climate simulations with different horizontal resolutions (Gu et al. 2020) also showed that RCMs could improve the regional climate simulations over the TP with higher resolution. Although RCMs have been proven to be useful tools to provide detailed regional climate information over the TP, they retain great deficiencies due to the complex terrain and the relatively coarse resolution (grid spacing > 10km) used. The cumulus parameterization, which is used to resolve the deep convection process at coarse resolution, has been identified as the major source of errors and uncertainties in the regional climate simulations over the TP (Ou et al. 2020). A promising remedy to the error-prone climate simulations using convective parameterizations is the use of convection-permitting model (CPM; horizontal grid spacing < 4km). It operates on the kilometer scale and no longer relies on convection parameterization schemes, which provides more reliable climate information on regional to local scales (Prein et al. 2015;Zhou et al. 2021). By resolving deep convection explicitly and improving the representation of orography and other surface forcing, the CPM climate simulations are able to improve the climatological mean temperature especially in mountainous regions during summer (Hohenegger et al. 2008; Prein et al. 2013a) and the diurnal cycle of summer precipitation. Using the WRF model, Gao et al. (2020) simulated the precipitation over the TP without reliable in-situ observations and found that the high-resolution CPM has the added value in reproducing the precipitation. Li et al. (2020) showed that the CPM could significantly reduce the wet bias in the coarse resolution simulations and better depict the precipitation frequency and intensity over the TP. Several CPM experiments have also been conducted over the TP to access the effect of physical options on the CPM performance (Ou et al. 2020; Lv et al. 2020), and to study the impact of resolution on the simulation of water vapor transport (Lin et al. 2018).

Traditionally, the regional climate downscaling commonly employs a continuous integration of the RCM driven by the global reanalysis or the global climate model (GCM) outputs, such as the GCM outputs from the Coupled Model Intercomparison Project (CMIP). However, due to the deficiency in the RCM structure and physics, the large-scale flow in the RCM simulation may departure from the driving fields, leading to the systematic model biases growth in long-term integrations. To prevent the RCMs from drifting away from the large scale forcing and ensure the model result consistent with the driving fields, several dynamical downscaling methods have been developed such as the re-initialization approach (RI) (Lo et al. 2008) and the spectral nudging technique (SN) (von Storch et al. 2000; Tang et al. 2011, 2016). The RI approach aims to mitigate the systematic error accumulation in the continuous long-term simulations through the consecutive or periodically reinitialized short-term runs (Qian et al. 2003). Usually, this approach can be carried out at different frequencies (e.g. daily, weekly or monthly). Lo et al. (2008) demonstrated that a run with more frequent re-initialization outperforms that with less frequent re-

initialization. Over the TP, the daily re-initialization approach was used to generate the High Asia Reanalysis (HAR) (Maussion et al. 2014; Wang et al. 2020), which showed added value in reproducing the spatial pattern and seasonality of precipitation. As a fake data assimilation technique, spectral nudging introduces the bias corrections of large scale circulation throughout the RCM domain rather than just limiting them to the initial and lateral boundary conditions, thus minimizing climate drift. Using the SN approach, Song et al. (2012) conducted a series of experiments in East Asia and the results revealed that SN could improve the simulation of precipitation due to the reduced bias of large-scale circulation field. Although both RI and SN approaches have been widely used in regional climate simulations, little work has been done to compare these two methods in convection-permitting (CP) scale simulations, especially over the TP regions with complex topography.

In this study, using the CP WRF model, we perform two experiments with different dynamical downscaling methods (RI and SN) over the TP in summer from 2016 to 2018. The simulated surface variables are compared with both the station observations and the satellite-derived dataset. The purpose of this study is to: (1) Evaluate the CPM's performance in reproducing the spatiotemporal characteristics of surface variables over the TP; (2) Identify the strengths and weaknesses of the two dynamical downscaling approaches in simulating the regional climate over the TP at CP scale. The paper is organized as follows. Section 2 briefly describes the model, data and methodology. Section 3 compares the models' simulations with the observations. Discussion and major conclusions are presented in Sect. 4 and Sect. 5.

2. Data, Model And Experimental Design

2.1 Model and experimental design

The WRF model version 4.1.1 (Skamarock et al. 2019), which is a nonhydrostatic mesoscale numerical weather prediction system designed to serve both operational forecasting and atmospheric research needs, is used in this study. It has been widely used in regional climate simulations around the world (Tang et al. 2016, 2017). The model domain in this work is centered at 33°N and 88.5°E, with 1081×721 grid points in east-west and north-south directions, covering the whole TP and the surrounding area (Fig. 1). Fifty hybrid-sigma levels are defined from surface to model top at 50hPa. The horizontal resolution is set to 3km for the convection-permitting scale simulation over the TP. To evaluate the skill of WRF in reproducing the regional climate over the TP in detail, four sub-regions are chosen from the whole study area based on the topography and climate features: the northwest region (TP-NW, 32.5°–37°N, 75°–91°E), the southwest region (TP-SW, 28°–32.5°N, 82°–91°E), the northeast region (TP-NE, 32.5°–39°N, 91°–102°E) and the northwest region (TP-SE, 28°–32.5°N, 91°–102°E).

The physical parameterization schemes employed in this research include the Thompson microphysics scheme (Thompson et al. 2008), the Mellor-Yamada Nakanishi Niino 2.5 level TKE scheme (MYNN) planetary boundary layer (PBL) parameterization (Nakanishi et al. 2006), the RRTMG shortwave and longwave radiation schemes (Iacono et al. 2008), and the Noah-MP land surface model (Niu et al. 2011).

With the horizontal resolution at CP scale (3km), the cumulus convection parameterization scheme is switched off.

Two sets of regional climate simulations are carried out, employing the spectral nudging scheme (hereinafter Exp-SN) and the re-initialization approach (hereinafter Exp-RI), respectively. In the SN approach, it is supposed that the regional climate model is forced to satisfy not only the boundary conditions, possibly in a boundary sponge region, but also the large-scale flow conditions inside the integration area (von Storch et al. 2000). The time-varying large-scale information with the wavenumber less than a preset value is nudged on the interior model domain in the SN experiment. In this study, the simulation domain is about 3200 km and 2200 km in zonal and meridional directions, respectively. The wavenumber of 4 is employed in both directions with the corresponding wave lengths about 800 km and 500 km, which means the forcing circulation information with the scale larger than the wave lengths can be nudged. Previous studies indicated that applying the SN to the horizontal winds showed good performance in reproducing the regional climate characteristics (Alexandru et al., 2009; Tang et al., 2010, 2016). In the Exp-SN simulation, SN is only applied to the wind fields above the PBL to allow the development of the mesoscale circulation. The Exp-RI consists of multiple consecutive reinitialized model runs with a 36-hour time integration. Each run starts at 12:00 UTC with the first 12 hours as the spin-up time, and the remaining 24 hours of the model outputs are used. By subdividing the long-term continuous integration into short ones, re-initialization has been successful in weather forecasting to mitigate the problem of systematic error growth in long integrations (Lo et al., 2008). Many studies had pointed out that the re-initialization approach could be beneficial to RCM simulations (Druyan et al. 2001; Qian et al. 2003). All the experiments are driven by the 4th generation Global Reanalysis data (ERA5) from European Centre for Medium-Range Weather Forecasts (ECMWF) (Hersbach et al., 2020), and simulate the summer climate (June, July and August, JJA) from 2016 to 2018. In the Exp-SN, the simulation starts from May 16 and integrates continuously to September 1 with the first 16 days (May 16–31) as the spin-up time.

2.2 Observation data and method

To evaluate the performance of the WRF model in simulating the surface climate over the TP at CP scale, two observation datasets are used. One is the daily in-situ observation provided by the data service center at China Meteorology Administration (CMA, http://data.cma.cn/en). Only 144 stations over the TP are applied in this study (Fig. 1b), which have comparatively applicable observations of daily surface air temperature (T2m), maximum/minimum surface air temperature (Tmax and Tmin) and precipitation. Most of the meteorological stations are located in the central and eastern part of the TP and few over the western TP. Therefore, the data from the meteorological stations cannot fully represent the TP, especially the western TP and the region above 4,800 m ASL (Qin et al. 2009). Thus, to validate the WRF-simulated precipitation and surface air temperature over the TP in detail, the satellite precipitation and surface air temperature products are also used to carry out a more objective evaluation.

The Global Satellite Mapping of Precipitation version 6 (GSMaP) products, operated by the Japan Aerospace Exploration Agency (JAXA), are used in this study. The spatiotemporal resolution of the GSMaP products is 0.1° × 0.1°and 1-hour. The gauge-adjusted GSMaP data (GSMaP-Gauge) is adopted

to evaluate the WRF simulations, which is a gauge-calibrated product by adjusting the GSMaP estimate using the National Oceanic and Atmospheric Administration (NOAA)/Climate Prediction Center (CPC) gauge-based analysis of global daily precipitation. Lu et al. (2018) demonstrated that the GSMaP-Gauge data showed comparable performance with the gauge reference data, suggesting that it can be selected for hydrological application over the TP.

A new long-term spatially and temporally continuous Moderate Resolution Imaging Spectroradiometer (MODIS) land surface temperature (LST) dataset for China from 2003 to 2017 (Zhao et al. 2020) is used to validate the WRF simulations. The temporal and spatial resolutions are monthly and 5600 m, respectively. It takes full advantages of the MODIS data and the meteorological station data by combing them to reconstruct real LST with the help of a regression analysis model. Thus, it makes up for the deficiency of sparse observation stations and effectively overcomes the limitations in reconstructing the real LST under cloudy conditions. The high-precision monthly LST dataset constructed for China is convinced to be highly consistent with the in-situ observation and provides detailed spatiotemporal patterns of LST. Therefore, it is suitable for analyzing the regional characteristics of LST at the annual, seasonal and monthly scales.

Several statistical measures are used to quantify the accuracy of the WRF simulations. The correlation coefficient and the root-mean-square error (RMSE) are calculated. The correlation coefficient is used to describe the temporal and spatial similarity between the observation and the simulation. The mean difference between the simulated and the observed climate variables can be described by the RMSE, regardless of the sign of the difference.

3. Results From The Re-initialization And Spectral Nudging Experiments

Evaluation of the WRF experiments using two regional climate simulation approaches (Exp-SN and Exp-RI) is performed through statistical verifications of mean and daily T2m and precipitation, as well as the diurnal variation of precipitation over the TP region. All the simulation results are interpolated to the station sites or the grid cells with the inverse distance weight interpolation method to be compared with the in-situ observations and the satellite precipitation products.

3.1 Summer mean surface air temperature and precipitation

Figure 2 shows the 3-yr averaged (2016–2018) summer mean daily T2m, Tmax and Tmin from the in-situ observations, and the differences between the WRF simulations and the observation. The observed T2m decreases from the southeast TP to the northwest, with the maximum T2m about 24°C in the eastern TP while the minimum T2m below 10°C in the central TP. All the WRF experiments can well produce the spatial pattern of T2m with the spatial correlation coefficients (SCCs) larger than 0.90, but tend to underestimate the T2m over the regions south of 35°N, especially in the Exp-RI with greater cold bias about − 5°C. The simulated distributions of Tmax and Tmin also agree well with the observations with the

SCCs above 0.86 and the RMSE below 3.60°C. Compared to the Exp-RI, the Exp-SN has lower RMSEs for the spatial patterns of T2m and Tmax. The daily temperature range (DTR) is higher over the regions north of 30°N according to the station observations (not shown), which is above 12°C, while the minimum DTR below 10°C is found over the southeastern TP. All the WRF experiments can well capture the spatial pattern of DTR with the SCCs higher than 0.73 and the RMSEs less than 2.31°C, and the Exp-SN shows a higher SCC of 0.78. However, they both show obvious cold bias over the central and northern TP, with the cold bias approximately 1°C in the Exp-SN and up to 3°C in the Exp-RI.

The summer mean LST is also evaluated against the satellite data. Figure 3 shows the summer mean LST from the MODIS dataset and the WRF experiments in 2016 and 2017, and the difference between the two years. According to the MODIS data, the warmer LST is located over the northeastern TP, with the maximum value above 24°C in the Qaidam Basin. The colder LST is located over the central TP and along the southern slope of TP with the minimum value below 4°C. All the WRF experiments can reproduce the spatial pattern of LST with the SCCs above 0.74 and the RMSEs below 4.6°C. The Exp-SN experiment generates warm biases of LST especially over the western and southern TP, with the RMSE larger than that in the Exp-RI when compared with the MODIS data. On the other hand, the Exp-SN agrees well with the MODIS data in simulating the difference of summer LST between 2016 and 2017, while the Exp-RI clearly overestimates the difference.

Figure 4 depicts the 3-yr averaged summer precipitation from the station observations and the GSMaP satellite dataset, and the biases in the WRF simulations. The observed precipitation decreases from the southeast TP to the northwest, with the maximum precipitation above 6 mm/day located at the southeastern corner of TP and along the southern slope of TP, while the minimum precipitation extending along the northwest of TP is below 1 mm/day. All the WRF experiments can well capture the spatial pattern of summer precipitation with the SCCs above 0.7 and the RMSEs below 1.16 mm/day when compared with the station observations, but they tend to underestimate the precipitation in most regions of TP with greater bias over the regions south of 35°N. Unlike the sparse station observations over the TP especially the western TP, the GSMaP dataset has a whole coverage over the TP with a high resolution. WRF shows higher SCCs (> 0.64) and comparable RMSEs when compared with the GSMaP precipitation dataset. The Exp-SN has small precipitation biases ranging from − 2 mm/day to 2 mm/day over most regions of TP. However, obvious wet bias (above 4 mm/day) exists over the central TP in the Exp-RI, which may accounts for the larger RMSEs and the lower SCCs than those in the Exp-SN.

The Taylor diagrams are presented to evaluate the two WRF experiments in simulating the spatial distributions of summer temperature and precipitation over the TP in each year (2016–2018) (Fig. 5). When compared with the station observations, the Exp-SN and the Exp-RI have similar performances in simulating the distributions of T2m, Tmax and Tmin with the SCCs about 0.90. For the precipitation, the two WRF experiments also show comparable performances when compared with the station observations. However, the Exp-SN outperforms the Exp-RI when the GSMaP precipitation dataset is used as a reference, with obviously higher SCC and lower RMSE in each year. Although there exist subtle differences in the simulation of precipitation between the two experiments when different datasets are

selected as references, they still show similar spatial patterns in most regions of TP, which promotes our understanding of summer precipitation over the TP.

3.2 Daily surface temperature and precipitation

The 3-yr averaged (2016–2018) daily variations of regional mean (over the TP) T2m, Tmax, Tmin and DTR from the in-situ observations, the Exp-SN and the Exp-RI are shown in Fig. 6. The observed T2m ranges from 10°C to 16°C throughout summertime, with the maximum T2m in late July and early August. All the WRF experiments can well simulate the daily variation of T2m with the temporal correlation coefficients (TCCs) higher than 0.95 and the RMSEs less than 1.33°C (Table 1). Although both experiments tend to underestimate the T2m in summer, the Exp-SN has lower RMSE. The Tmax ranges from 18°C to 24°C in the observation, and the model shows similar simulation ability to that for the T2m, with the TCCs above 0.97 and the RMSEs less than 2.88°C. For the Tmin, both experiments exhibit better simulation than that of Tmax, with lower RMSEs. The observed DTR varies between 9°C and 18°C, with the maximum DTR exceeding 16°C in early June and the minimum below 10°C in early July. The Exp-SN-simulated DTR is closer to the observation, with lower RMSE at about 1.0°C. Regarding the daily variation of regional averaged precipitation over the TP (Fig. 7), both Exp-SN and Exp-RI can catch its main characteristics with the TCCs all above 0.87. The two experiments have comparable performance when compared with the station observations. While with the GSMaP as the observation, the two experiments clearly overestimate the daily precipitation, and the Exp-SN can improve the simulation with lower RMSE.

Table 1
TCCs and RMSEs for the regional mean daily temperature and precipitation in the two experiments

	Exp-SN		**Exp-RI**	
	RMSE	TCC	RMSE	TCC
T2m	0.78	0.99	1.33	0.99
Tmax	1.73	0.98	2.88	0.97
Tmin	1.02	0.95	0.96	0.96
DTR	1.00	0.89	2.11	0.92
Precipitation (compared with station observation)	0.93	0.89	0.78	0.86
Precipitation (compared with GSMaP)	0.80	0.85	1.10	0.84

The spatial distributions of TCCs and RMSEs of T2m, Tmax and Tmin are presented in Figs. 8 and 9, respectively. The TCCs of T2m and Tmax demonstrate similar patterns in both experiments, decreasing from northeast to southwest, with the TCCs above 0.9 mostly occurring over the northeast TP and those

below 0.7 along the south slope of TP. The TCC of Tmin is lower than that of T2m and Tmax, ranging from 0.6 to 0.8 with less spatial variation. The RMSE of T2m is within 2°C over most regions in the Exp-SN, but it is larger in the Exp-RI, with the RMSE above 3.5°C at more stations over the regions south of 35°N. The RMSE of Tmax is greater than that of T2m and Tmin in both experiments, especially in the Exp-RI, with the maximum RMSE exceeding 5°C. The two experiments exhibit quite similar spatial patterns of RMSE for the Tmin, mostly ranging from 1°C to 3°C, which indicates their similar performance in simulating the Tmin.

Figure 10 and Fig. 11 show the spatial distributions of TCC and RMSE for the simulated daily precipitation. When compared with the station observations (Fig. 10), the two experiments demonstrate quite similar spatial patterns of TCC and RMSE. The TCCs above 0.5 are mainly located over the eastern TP, while the larger RMSEs mainly exist over the southeastern TP. With the GSMaP dataset as the observation (Fig. 11), it is also clear that the experiments demonstrate higher TCCs over the eastern TP, and the Exp-RI slightly improves the TCCs over the eastern TP. There are large precipitation RMSEs exceeding 9 mm/day over the southeastern and central TP, and along the south slope of TP. The RMSEs decrease from southeast to northwest, with the lowest RMSEs less than 1 mm/day over the western TP and the Qaidam Basin. Compared with the Exp-RI experiment, the Exp-SN significantly reduces the RMSEs of daily precipitation variation over the central TP and part of the eastern TP, with reduction of RMSE about 3 mm/day over the central TP.

3.3 Diurnal cycle of precipitation

To evaluate the performance of WRF in simulating the diurnal variation of precipitation over the TP, the GSMaP satellite precipitation dataset with the temporal resolution of 1-hour is used as the observation. Figure 12 shows the 3-yr averaged (2016–2018) occurrence time of maximum precipitation from the observation and the Exp-SN and Exp-RI experiments. The observed maximum precipitation mostly occurs after 18:00 Local Standard Time (LST) over the TP, and even after 22:00 LST over the southeastern TP, while it mainly occurs in early morning in the Qaidam Basin. All the WRF experiments can well produce the spatial pattern of the occurrence time of maximum precipitation over the eastern TP with 1 to 2 hours in advance. However, they all tend to simulate a much more advanced occurrence time of maximum precipitation over the southeastern TP and along the south slope of TP. The greatest difference between the Exp-SN and the Exp-RI lies over the western TP. The maximum precipitation in the Exp-SN occurs before 06:00 LST over most regions of western TP, while the simulation of Exp-RI agrees more with the observation.

Figure 13 shows the 3-yr averaged regional mean diurnal cycle of precipitation amount (PA) over the whole TP, TP-NW, TP-SW, TP-NE and TP-SE. It can be found that the observed PA ranges from 0.05 to 0.2 mm/hr over the TP, with the two peaks occurring at 17:00 LST and 22:00 LST. Both Exp-SN and Exp-RI can well capture the bimodal structure of the diurnal variation of precipitation over the TP, but they all tend to simulate the precipitation peak at 17:00 LST in advance by 1 hour and postpone the peak at 22:00 LST by 3 hours. The Exp-SN can reduce the wet bias in the Exp-RI, especially at night and in early

morning. Over TP-SE and TP-SW, the observed diurnal variations of PA are quite similar, with two peaks in the afternoon (about 16:00 LST) and at night (about 22:00 LST), respectively. Both Exp-SN and Exp-SI can generally reproduce the diurnal cycle, but they all simulate the peak in the afternoon about 3 hours earlier than the observation. The Exp-SN can catch the bimodal structure of the diurnal cycle over TP-SE and well simulate the PA peak at night, while the Exp-RI only simulates a unimodal structure and cannot capture the PA peak at night. The two experiments can reproduce the diurnal cycle of PA over TP-NE with the peak in the afternoon, while the Exp-RI clearly overestimates the daytime PA. Over TP-NW, the precipitation amount is weaker than that in the other sub-regions. Although the WRF experiments can simulate the diurnal variations of PA, they all significantly overestimate the PA especially in the afternoon and at night. The diurnal variations of precipitation frequency (PF) are quite similar to those of PA (figure not shown), and both Exp-SN and Exp-RI can reproduce the diurnal cycles with obvious nocturnal precipitation. The WRF model tends to overestimate the PF over the whole TP, especially over TP-SE and TP-NW, indicating that the overestimation of PA over the TP may be induced by the overestimation of PF.

In general, both WRF experiments can well reproduce the spatial pattern of the occurrence time of maximum precipitation and the diurnal cycle of precipitation over the TP, especially over the eastern TP. The WRF model tends to overestimate the PF over the TP, which leads to the overestimation of PA.

4. Discussion

To investigate into the causes of the differences between Exp-SN and Exp-RI in simulating the temperature over the TP, the 3-yr averaged surface net radiation and the sum of sensible heat and latent heat fluxes at 06:00 and 18:00 UTC are plotted in Fig. 14. It can be found that the surface net radiation in the Exp-SN is larger than that in the Exp-RI at 06:00 UTC. It is greater than 570 W/m^2 in most regions over TP in the Exp-SN experiment at 06:00 UTC, while below 540 W/m^2 in the Exp-RI experiment. The surplus surface net radiation in the Exp-SN mainly comes from the downward shortwave radiation, which is about 100 W/m^2 larger than that in the Exp-RI. Meanwhile, the sum of sensible and latent heat fluxes from surface in the Exp-SN is a little smaller than that in the Exp-RI at 06:00 UTC. The larger surface net radiation and the smaller upward heat fluxes in the Exp-SN at 06:00 UTC lead to the warmer daily maximum surface air temperature. At nighttime (18:00 UTC), the surface net radiation mainly comes from the longwave radiation cooling, and both Exp-SN and Exp-RI show negative values in most regions of TP. The Exp-SN produces a little smaller surface net radiation than the Exp-RI over the southeastern TP. The sum of sensible and latent heat fluxes in both experiments shows similar spatial pattern. Therefore, the difference of surface air temperature at night (Tmin) between Exp-SN and Exp-RI is quite small. It is natural to deduce that the energy balance at daytime results in the warmer mean surface air temperature in the Exp-SN experiment.

Atmospheric water vapor is very important to precipitation. Figure 15 shows the 3-yr averaged moisture flux divergence at low level (500hPa) over the TP in the two experiments. In both Exp-SN and Exp-RI experiments, vigorous moisture convergence and divergence occur over the northwestern TP and along the south slope of TP, which is stronger in the Exp-RI. Over the central TP where wetter bias occurs in the

Exp-RI, stronger moisture flux convergence can be found in the Exp-RI compared with the Exp-SN. Furthermore, the larger upward latent heat flux in the Exp-RI indicates more water vapor transported from surface over the central and eastern TP. Thus, the stronger moisture flux convergence and the more water vapor lead to more precipitation and greater wet biases in the Exp-RI experiment.

5. Conclusions

Two WRF experiments with the regional climate simulation schemes of spectral nudging and re-initialization are performed over the TP. The surface air temperature and the precipitation are evaluated based on the in-situ station observations and the GSMaP dataset.

Both WRF experiments successfully capture the spatial patterns and the daily variations of T2m and Tmax, with the SCCs and the TCCs over 0.85 and 0.95, respectively. The spatiotemporal characteristics of Tmin are also reasonably reproduced. The DTR is underestimated over southern TP in summer in both experiments, with the biases smaller and the SCC higher in the Exp-SN. Warm biases are produced for the LST, especially in the Exp-SN over western and southern TP, while the difference of summer LST between 2016 and 2017 is better simulated in the Exp-SN. The surface energy budget is further analyzed, indicating that the surplus surface net radiation coming from the downward shortwave radiation and the insufficient upward heat fluxes at daytime result in the higher surface air temperature in the Exp-SN. On the other hand, the similar spatial distribution of sensible and latent heat fluxes at nighttime in the two experiments leads to the negligible difference in the simulated Tmin.

The spatial pattern and the daily variation of summer precipitation are also reasonably reproduced in both WRF experiments, with the SCCs and the TCCs above 0.7 and 0.86, respectively. However, dry bias exists in the regions south of 35°N in summer, which is consistent with the cold bias of temperature. Based on the GSMaP dataset, dominant wet biases are found in both experiments, which is smaller in the Exp-SN. The opposite bias reminds us that validations of model simulation against observational data should be considered with care, especially when the datasets come from different sources. The further investigation into the 500-hPa circulation indicates that the stronger moisture flux convergence together with the more water vapor transported from surface leads to more precipitation and thus greater wet biases in the Exp-RI experiment.

The diurnal cycle of precipitation over the TP is explored to better understand its temporal variation. Both WRF experiments can well produce the spatial pattern of the occurrence time of maximum precipitation over eastern TP, despite an advance of 1–2 hours in the simulations. Over western TP, the Exp-RI performs better than the Exp-SN. In addition, the diurnal cycles of PA and PF are reasonably simulated in both experiments, with the obvious nocturnal precipitation well captured, however, the precipitation peak at 17:00 LST is produced in advance and that at 22:00 LST is postponed. The WRF model tends to overestimate the PF over the whole TP, especially over TP-SE and TP-NW, which indicates that the greater overestimation of PA in the Exp-RI may be induced by the overestimation of PF.

The re-initialization scheme has been proved to be a favorable approach for RCM simulations (Druyan et al. 2001; Qian et al. 2003). This study reveals that the spectral nudging scheme is also a competitive approach, since the Exp-SN and the Exp-RI demonstrate comparable performances in the simulations of temperature and precipitation over the TP. The results in this research can provide a better understanding of the climate in recent years over the TP.

Declarations

Acknowledgments:

The research is supported by the Second Tibetan Plateau Scientific Expedition and Research Program (STEP, Grant No.2019QZKK0206) and National Key Research and Development Program of China (2018YFA0606003), as well as the National Natural Science Foundation of China (41875124).

Authors' contributions:

All authors contributed to the study conception and design. Material preparation, data collection and analysis were performed by Mengnan Ma, Peifeng Zhou and Jianping Tang. Pinhong Hui, Dongqing Liu and Jianping Tang helped perform the analysis with constructive discussions. The first draft of the manuscript was written by Mengnan Ma and all authors commented on previous versions of the manuscript. All authors read and approved the final manuscript.

Funding:

This work was supported by the Second Tibetan Plateau Scientific Expedition and Research Program (STEP, Grant No.2019QZKK0206) and National Key Research and Development Program of China (2018YFA0606003), as well as the National Natural Science Foundation of China (41875124).

Availability of data and material

The station observations used in this work are available at: http://data.cma.cn/en.

The GSMap satellite dataset is available at: https://sharaku.eorc.jaxa.jp/GSMaP/

The combined Terra and Aqua MODIS land surface temperature and meteorological station data product for China is available at: https://data.tpdc.ac.cn/en/data/055dfa65-e097-4000-9bda-992def32969f/?q=

Code availability

The analysis code is available on request from the corresponding author.

Conflicts of interest

The authors have no conflicts of interest to declare that are relevant to the content of this article.

Consent to participate

Written informed consent was obtained from all participants.

Consent for publication

Written informed consent for publication was obtained from all participants.

References

1. Alexandru A, De Elia R, Laprise R et al (2009) Sensitivity study of regional climate model simulations to large-scale nudging parameters[J]. Mon Weather Rev 137(5):1666–1686
2. Druyan LM, Fulakeza M, Lonergan P et al (2001) A regional model study of synoptic features over West Africa[J]. Monthly weather review 129(6):1564–1577
3. Duan AM, Wu GX (2005) Role of the Tibetan Plateau thermal forcing in the summer climate patterns over subtropical Asia[J]. Climate dynamics 24(7–8):793–807
4. Gao Y, Chen F, Jiang Y (2020) Evaluation of a convection-permitting modeling of precipitation over the Tibetan Plateau and its influences on the simulation of snow-cover fraction[J]. J Hydrometeorol 21(7):1531–1548
5. Gao Y, Xu J, Chen D (2015) Evaluation of WRF mesoscale climate simulations over the Tibetan Plateau during 1979–2011[J]. J Clim 28(7):2823–2841
6. Gu H, Yu Z, Peltier WR et al (2020) Sensitivity studies and comprehensive evaluation of RegCM4. 6.1 high-resolution climate simulations over the Tibetan Plateau[J]. Clim Dyn 54(7–8):3781–3801
7. Hersbach H, Bell B, Berrisford P et al (2020) The ERA5 global reanalysis[J]. Q J R Meteorol Soc 146(730):1999–2049
8. Hohenegger C, Brockhaus P, Schar C (2008) Towards climate simulations at cloud-resolving scales[J]. Meteorol Z 17(4):383–394
9. Iacono MJ, Delamere JS, Mlawer EJ et al (2008) Radiative forcing by long-lived greenhouse gases: Calculations with the AER radiative transfer models[J]. Journal of Geophysical Research: Atmospheres 113:D13
10. Ji Z, Kang S (2013) Double-nested dynamical downscaling experiments over the Tibetan Plateau and their projection of climate change under two RCP scenarios[J]. Journal of the atmospheric sciences 70(4):1278–1290
11. Kang S, Xu Y, You Q et al (2010) Review of climate and cryospheric change in the Tibetan Plateau[J]. Environmental research letters 5(1):015101
12. Li P, Furtado K, Zhou T et al (2020) Convection-permitting modelling improves simulated precipitation over the central and eastern Tibetan Plateau[J]. Quarterly Journal of the Royal Meteorological Society

13. Lin C, Chen D, Yang K et al (2018) Impact of model resolution on simulating the water vapor transport through the central Himalayas: implication for models' wet bias over the Tibetan Plateau[J]. Climate dynamics 51(9):3195–3207
14. Lo JCF, Yang ZL, Pielke Sr RA (2008) Assessment of three dynamical climate downscaling methods using the Weather Research and Forecasting (WRF) model[J]. Journal of Geophysical Research: Atmospheres 113:D9
15. Lu D, Yong B. Evaluation and hydrological utility of the latest GPM IMERG V5 and GSMaP V7 precipitation products over the Tibetan Plateau[J]. Remote Sensing, 2018, 10(12): 2022
16. Lv M, Xu Z, Yang ZL. Cloud resolving WRF simulations of precipitation and soil moisture over the central Tibetan Plateau: an assessment of various physics options[J]. Earth and Space Science, 2020, 7(2): e2019EA000865
17. Maussion F, Scherer D, Mölg T et al (2014) Precipitation seasonality and variability over the Tibetan Plateau as resolved by the High Asia Reanalysis[J]. J Clim 27(5):1910–1927
18. Nakanishi M, Niino H (2006) An improved Mellor–Yamada level-3 model: Its numerical stability and application to a regional prediction of advection fog[J]. Bound-Layer Meteorol 119(2):397–407
19. Niu GY, Yang ZL, Mitchell KE et al (2011) The community Noah land surface model with multiparameterization options (Noah-MP): 1. Model description and evaluation with local-scale measurements[J]. Journal of Geophysical Research: Atmospheres 116:D12
20. Ou T, Chen D, Chen X et al (2020) Simulation of summer precipitation diurnal cycles over the Tibetan Plateau at the gray-zone grid spacing for cumulus parameterization[J]. Clim Dyn 54(7):3525–3539
21. Pan BT, Li JJ, Chen FH. Qinghai-Xizang Plateau—a driver and amplifier of the global climatic change J[J]. Lanzhou University (Natural Science Edition), 1996, 32: 08-115. Prein AF, Gobiet A, Suklitsch M et al. Added value of convection permitting seasonal simulations[J]. Climate Dynamics, 2013, 41(9–10): 2655–2677
22. Prein AF, Langhans W, Fosser G et al (2015) A review on regional convection-permitting climate modeling: Demonstrations, prospects, and challenges[J]. Reviews of geophysics 53(2):323–361
23. Qian JH, Seth A, Zebiak S (2003) Reinitialized versus continuous simulations for regional climate downscaling[J]. Mon Weather Rev 131(11):2857–2874
24. Qin J, Yang K, Liang S et al (2009) The altitudinal dependence of recent rapid warming over the Tibetan Plateau[J]. Clim Change 97(1–2):321
25. Skamarock WC, Klemp JB, Dudhia J, Gill DO, Liu Z, Berner J, Wang W, Powers JG, Duda MG, Barker DM, Huang X-Y, 2019: A Description of the Advanced Research WRF Version 4. NCAR Tech. Note NCAR/TN-556 + STR, 145 pp
26. doi:10.5065/1dfh-6p97
27. Song S, Tang J, Chen X (2011) Impacts of spectral nudging on the sensitivity of a regional climate model to convective parameterizations in East Asia[J]. Acta Meteorologica Sinica 25(1):63–77

28. Su F, Duan X, Chen D et al (2013) Evaluation of the global climate models in the CMIP5 over the Tibetan Plateau[J]. J Clim 26(10):3187–3208
29. Tang J, Niu X, Wang S et al (2016) Statistical downscaling and dynamical downscaling of regional climate in China: Present climate evaluations and future climate projections[J]. Journal of Geophysical Research: Atmospheres 121(5):2110–2129
30. Tang J, Song S, Wu J (2010) Impacts of the spectral nudging technique on simulation of the East Asian summer monsoon[J]. Theoretical applied climatology 101(1–2):41–51
31. Tang J, Wang S, Niu X et al (2017) Impact of spectral nudging on regional climate simulation over CORDEX East Asia using WRF[J]. Clim Dyn 48(7–8):2339–2357
32. Thompson G, Field PR, Rasmussen RM, Hall WD (2008) Explicit Forecasts of Winter Precipitation Using an Improved Bulk Microphysics Scheme. Part II: Implementation of a New Snow Parameterization. Mon Wea Rev 136:5095–5115
33. von Storch H, Langenberg H, Feser F (2000) A spectral nudging technique for dynamical downscaling purposes[J]. Monthly weather review 128(10):3664–3673
34. Wang X, Tolksdorf V, Otto M et al. WRF-based Dynamical Downscaling of ERA5 Reanalysis Data for High Mountain Asia: Towards a New Version of the High Asia Refined Analysis[J]. International Journal of Climatology
35. Wang X, Yang M, Wan G et al (2013) Qinghai-Xizang (Tibetan) Plateau climate simulation using the regional climate model RegCM3[J]. Climate research 57(3):173–186
36. Yeh TC, Gao YX (1979) Meteorology of the Qinghai-Xizang (Tibet) Plateau[J]. Science, Beijing, p 278
37. You Q, Fraedrich K, Ren G et al (2012) Inconsistencies of precipitation in the eastern and central Tibetan Plateau between surface adjusted data and reanalysis[J]. Theoretical applied climatology 109(3–4):485–496
38. Zhao B, Mao K, Cai Y et al (2020) A combined Terra and Aqua MODIS land surface temperature and meteorological station data product for China from 2003 to 2017[J]. Earth System Science Data 12(4):2555–2577
39. Zhou X, Yang K, Ouyang L, et al. Added value of kilometer-scale modeling over the third pole region: a CORDEX-CPTP pilot study[J]. Climate Dynamics, 2021(599)

Figures

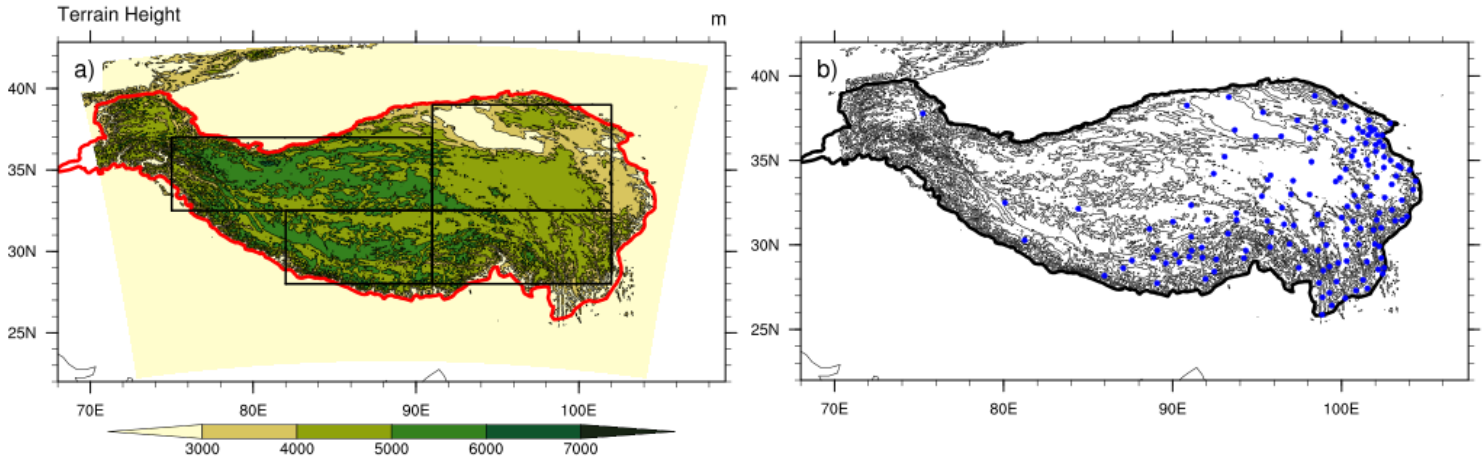

Figure 1

The simulation domain (yellow shading) with the TP framed with red lines and four sub-regions framed with black lines (a), and the locations of the meteorological stations within the simulation domain (b). Note: The designations employed and the presentation of the material on this map do not imply the expression of any opinion whatsoever on the part of Research Square concerning the legal status of any country, territory, city or area or of its authorities, or concerning the delimitation of its frontiers or boundaries. This map has been provided by the authors.

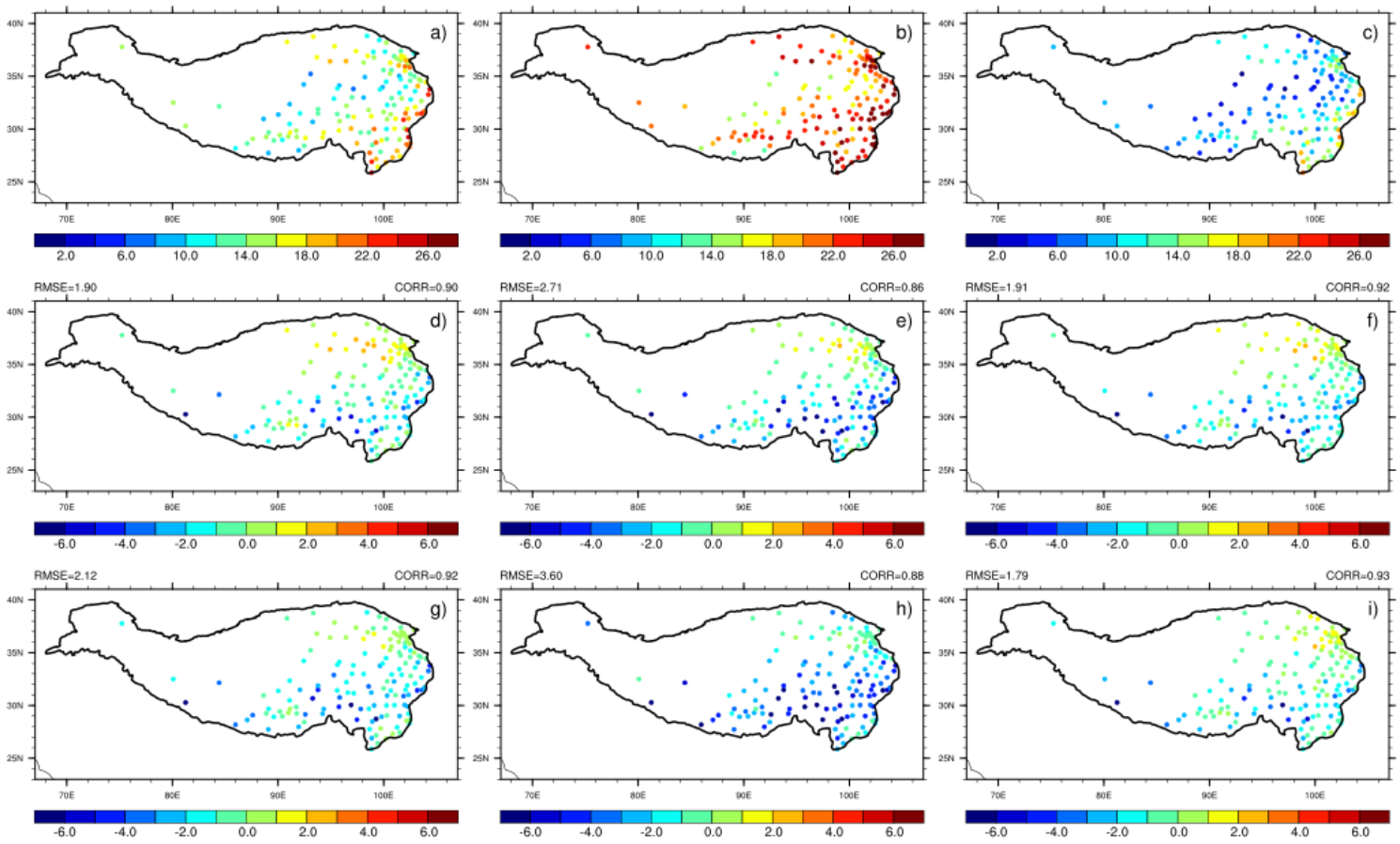

Figure 2

The 3-yr averaged (2016-2018) summer mean T2m, Tmax and Tmin from the in-situ observations (a, b, c), and the biases in the Exp-SN (d, e, f) and the Exp-RI (g, h, i). Units: °C. Note: The designations employed and the presentation of the material on this map do not imply the expression of any opinion whatsoever on the part of Research Square concerning the legal status of any country, territory, city or area or of its authorities, or concerning the delimitation of its frontiers or boundaries. This map has been provided by the authors.

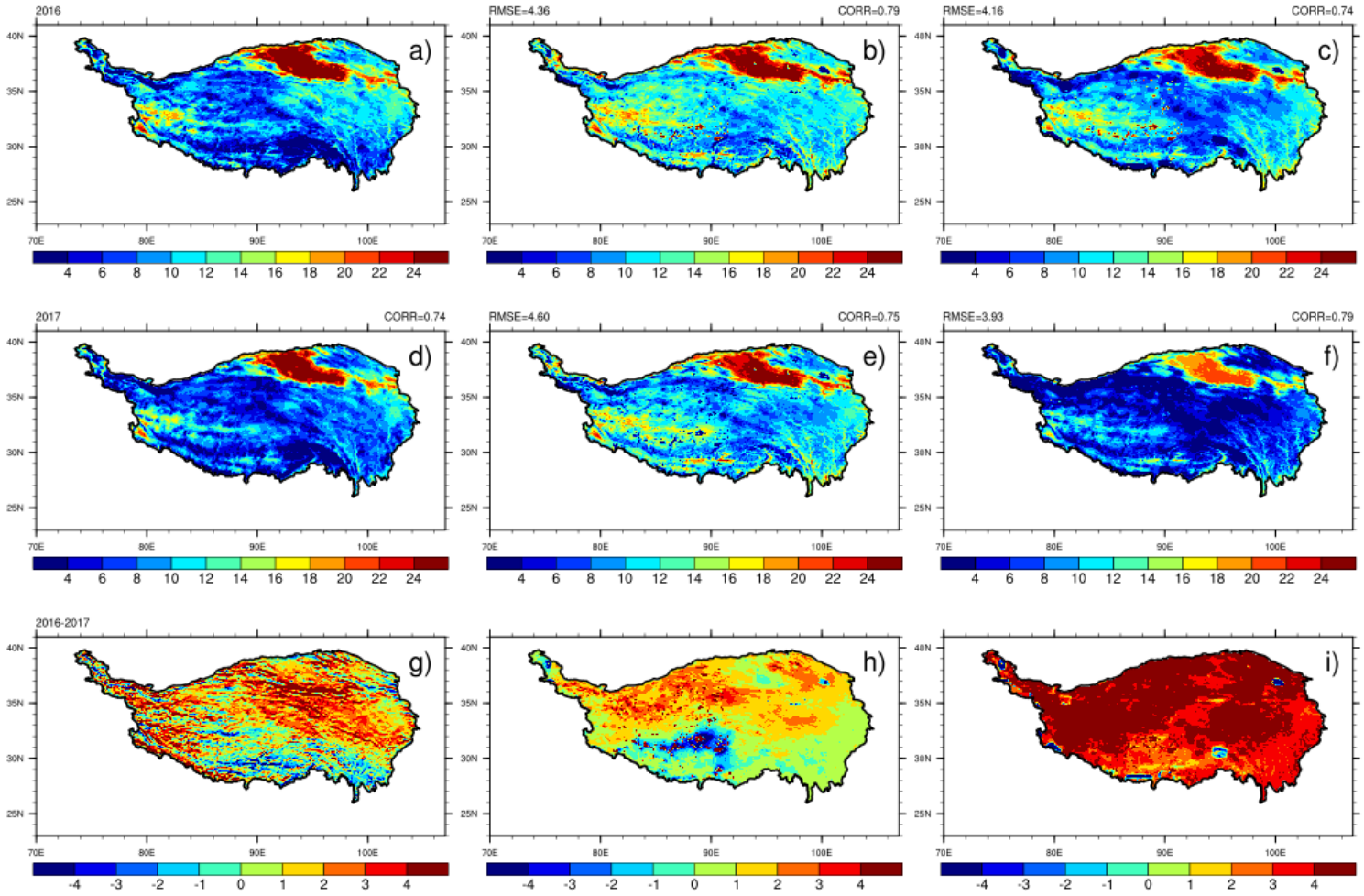

Figure 3

The 2016 and 2017 summer mean LST from the MODIS dataset (a, d), the Exp-SN (b, e) and the Exp-RI (c, f), and the difference of summer LST between 2016 and 2017 in the MODIS dataset (g), the Exp-SN (h) and the Exp-RI (i). Units: °C. Note: The designations employed and the presentation of the material on this map do not imply the expression of any opinion whatsoever on the part of Research Square concerning the legal status of any country, territory, city or area or of its authorities, or concerning the delimitation of its frontiers or boundaries. This map has been provided by the authors.

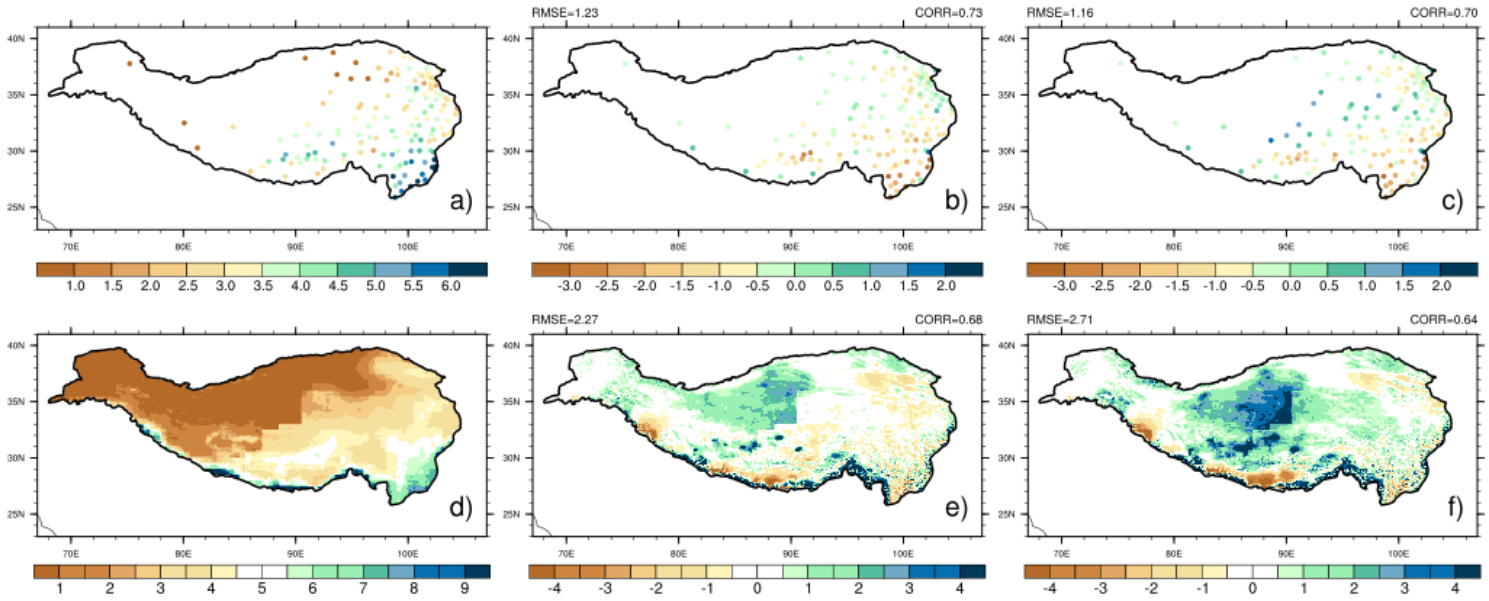

Figure 4

3-yr averaged summer precipitation from the station observations (a) and the GSMaP satellite dataset (d), and the biases in the Exp-SN and the Exp-RI compared with the station observation (b, c) and the GSMaP dataset (e, f). Units: mm/day. Note: The designations employed and the presentation of the material on this map do not imply the expression of any opinion whatsoever on the part of Research Square concerning the legal status of any country, territory, city or area or of its authorities, or concerning the delimitation of its frontiers or boundaries. This map has been provided by the authors.

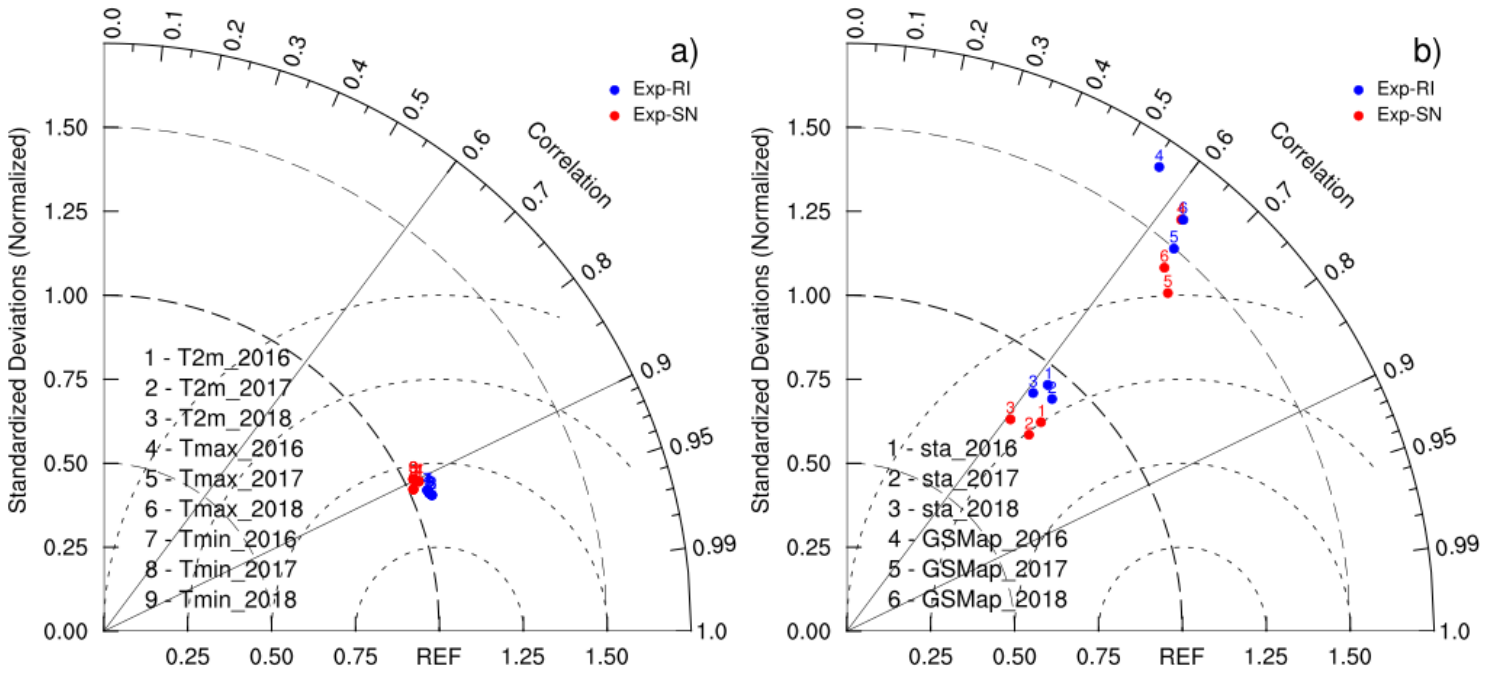

Figure 5

Taylor diagrams for the temperature (a) and the precipitation (b) from 2016 to 2018

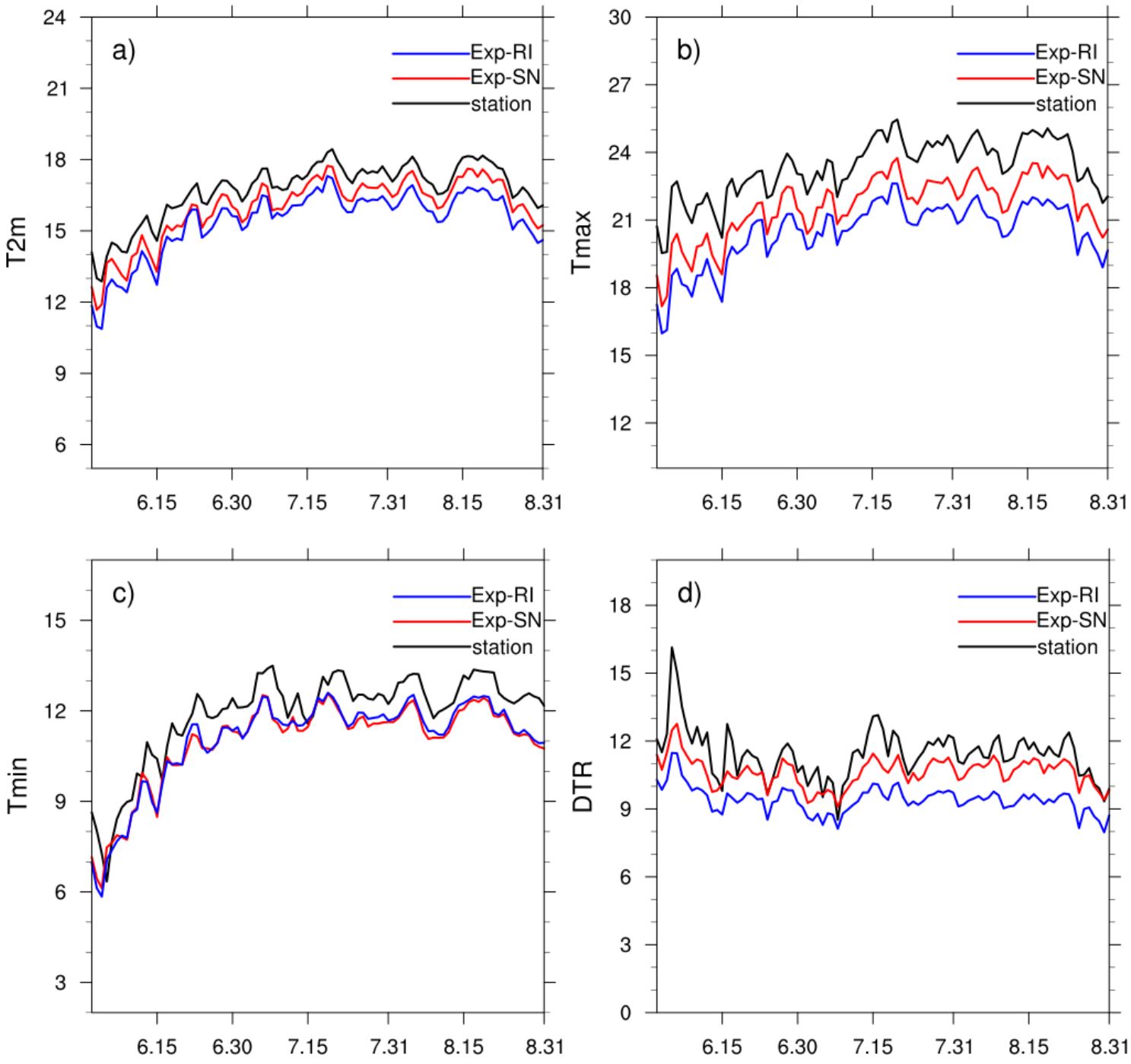

Figure 6

3-yr averaged daily variations of regional mean T2m (a), Tmax (b), Tmin (c) and DTR (d) from the in-situ observations and the simulations of Exp-SN and Exp-RI

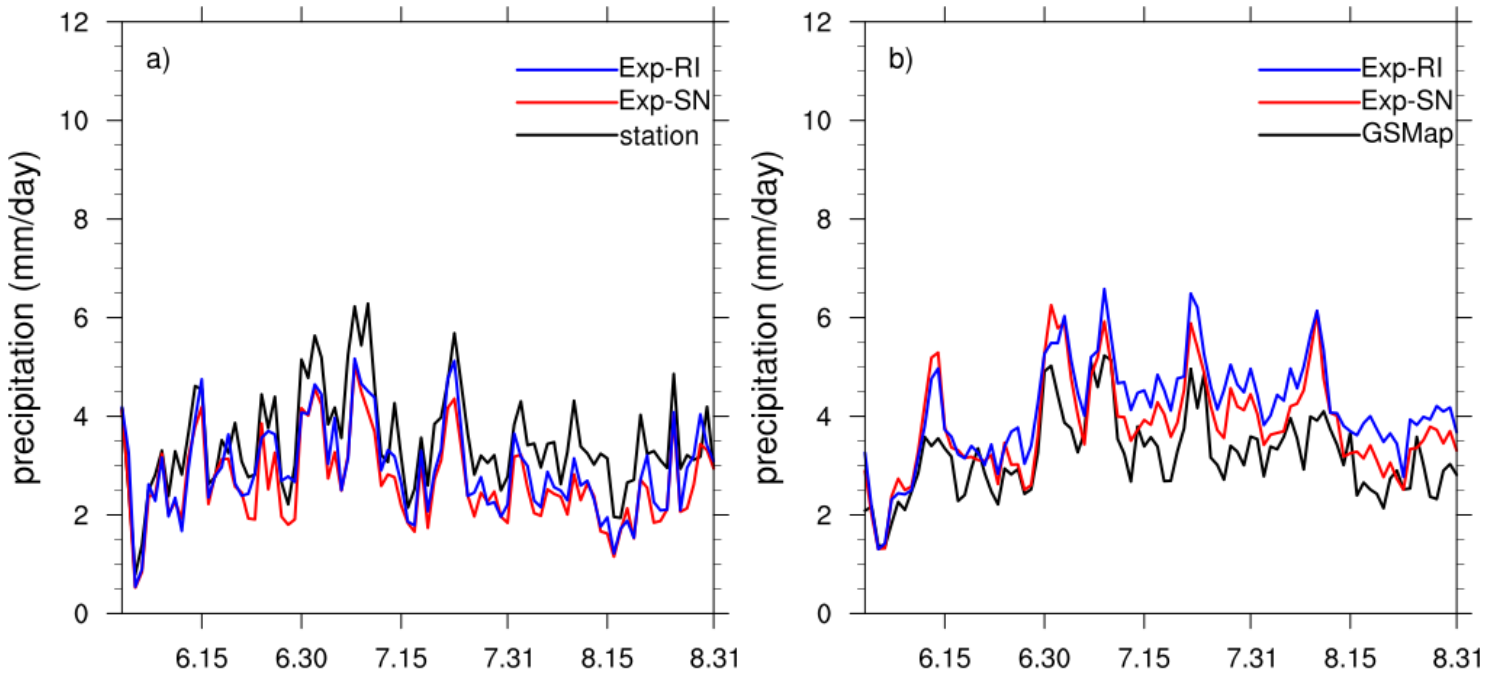

Figure 7

3-yr averaged daily variation of regional mean precipitation over the TP from the station observation (a) and the GSMaP dataset (b) accompanied with that in the WRF experiments

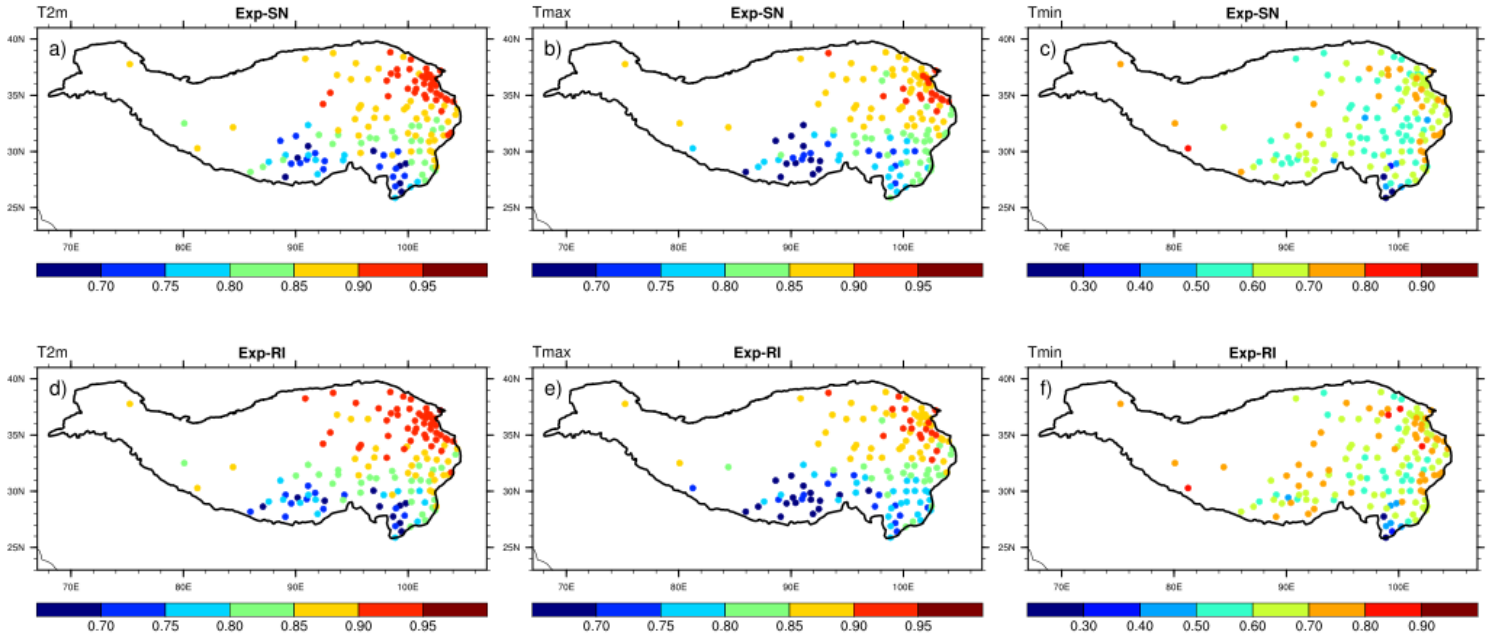

Figure 8

The spatial distributions of TCCs for the simulated T2m, Tmax and Tmin in the Exp-SN (a, b, c) and the Exp-RI (d, e, f). Note: The designations employed and the presentation of the material on this map do not imply the expression of any opinion whatsoever on the part of Research Square concerning the legal status of any country, territory, city or area or of its authorities, or concerning the delimitation of its frontiers or boundaries. This map has been provided by the authors.

Figure 9

Same as Fig 8, but for RMSEs. Note: The designations employed and the presentation of the material on this map do not imply the expression of any opinion whatsoever on the part of Research Square concerning the legal status of any country, territory, city or area or of its authorities, or concerning the delimitation of its frontiers or boundaries. This map has been provided by the authors.

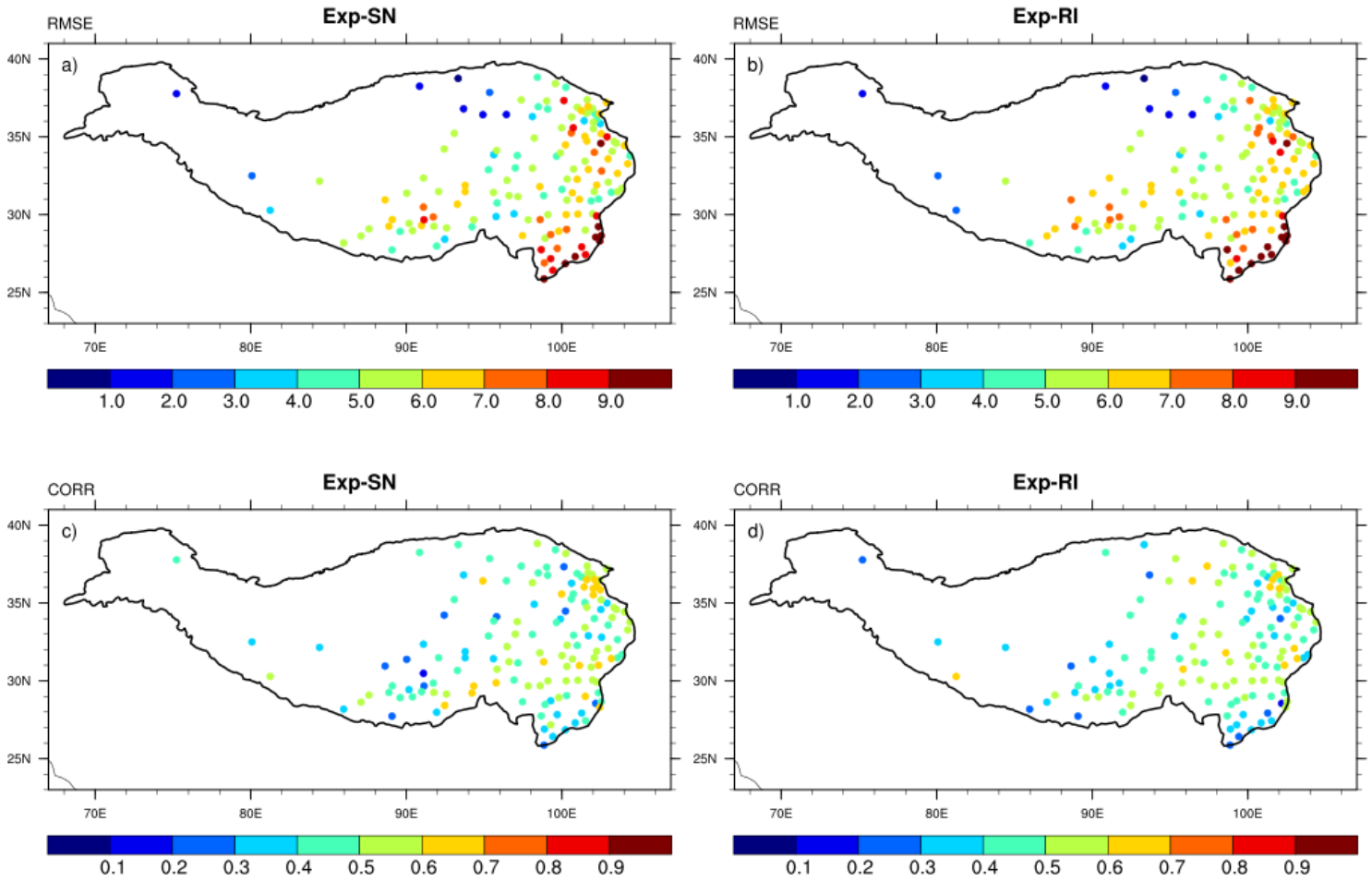

Figure 10

The spatial distributions of RMSEs (a, b) and TCCs (c, d) for the simulated daily precipitation compared with the station observations. Note: The designations employed and the presentation of the material on this map do not imply the expression of any opinion whatsoever on the part of Research Square concerning the legal status of any country, territory, city or area or of its authorities, or concerning the delimitation of its frontiers or boundaries. This map has been provided by the authors.

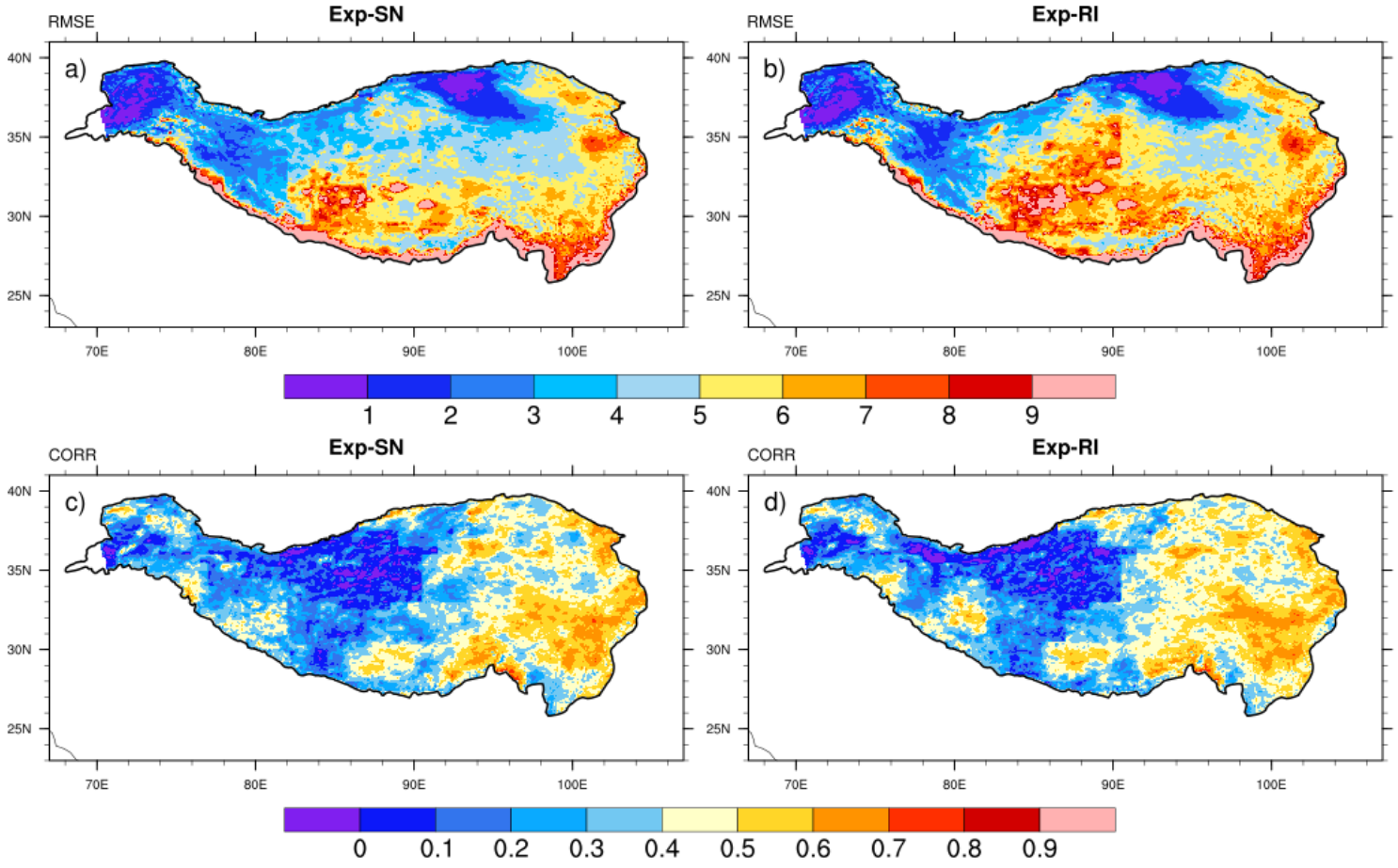

Figure 11

Same as Fig. 10, but compared with the GSMaP. Note: The designations employed and the presentation of the material on this map do not imply the expression of any opinion whatsoever on the part of Research Square concerning the legal status of any country, territory, city or area or of its authorities, or concerning the delimitation of its frontiers or boundaries. This map has been provided by the authors.

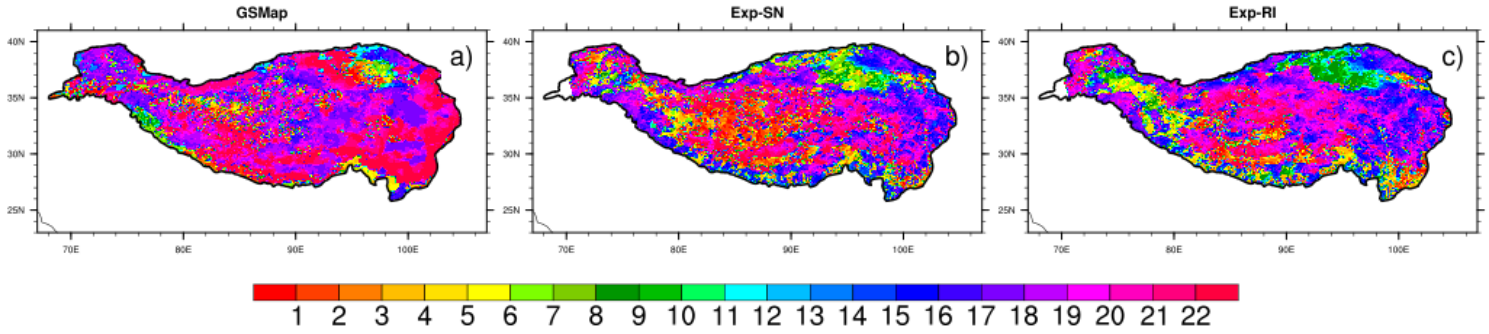

Figure 12

3-yr averaged occurrence time of maximum precipitation in the observation (a) and the WRF experiments (b, c). Note: The designations employed and the presentation of the material on this map do not imply the

expression of any opinion whatsoever on the part of Research Square concerning the legal status of any country, territory, city or area or of its authorities, or concerning the delimitation of its frontiers or boundaries. This map has been provided by the authors.

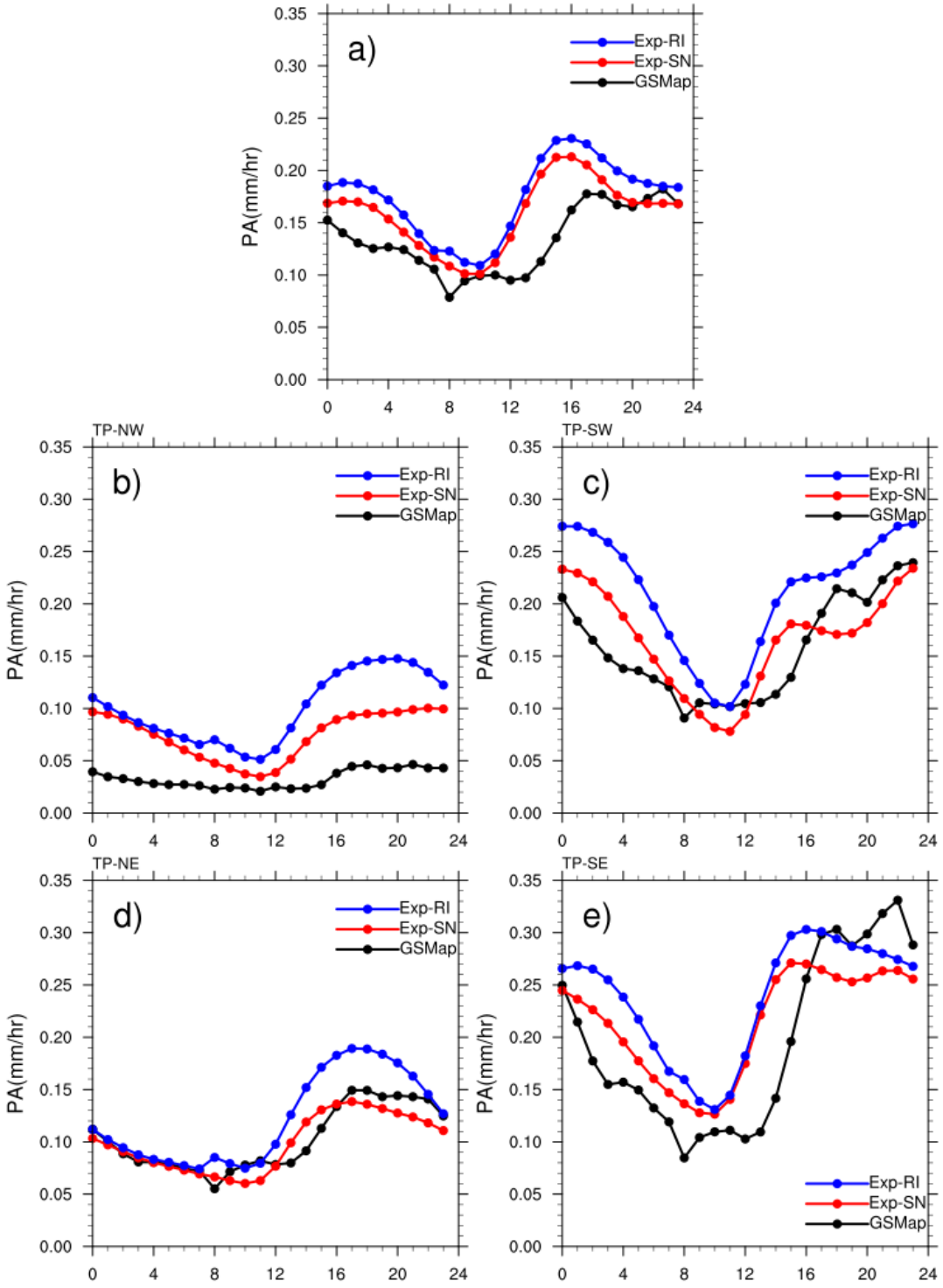

Figure 13

3-yr averaged regional mean diurnal cycle of precipitation amount (PA) over the whole TP (a), TP-NW (b), TP-SW (c), TP-NE (d) and TP-SE (e)

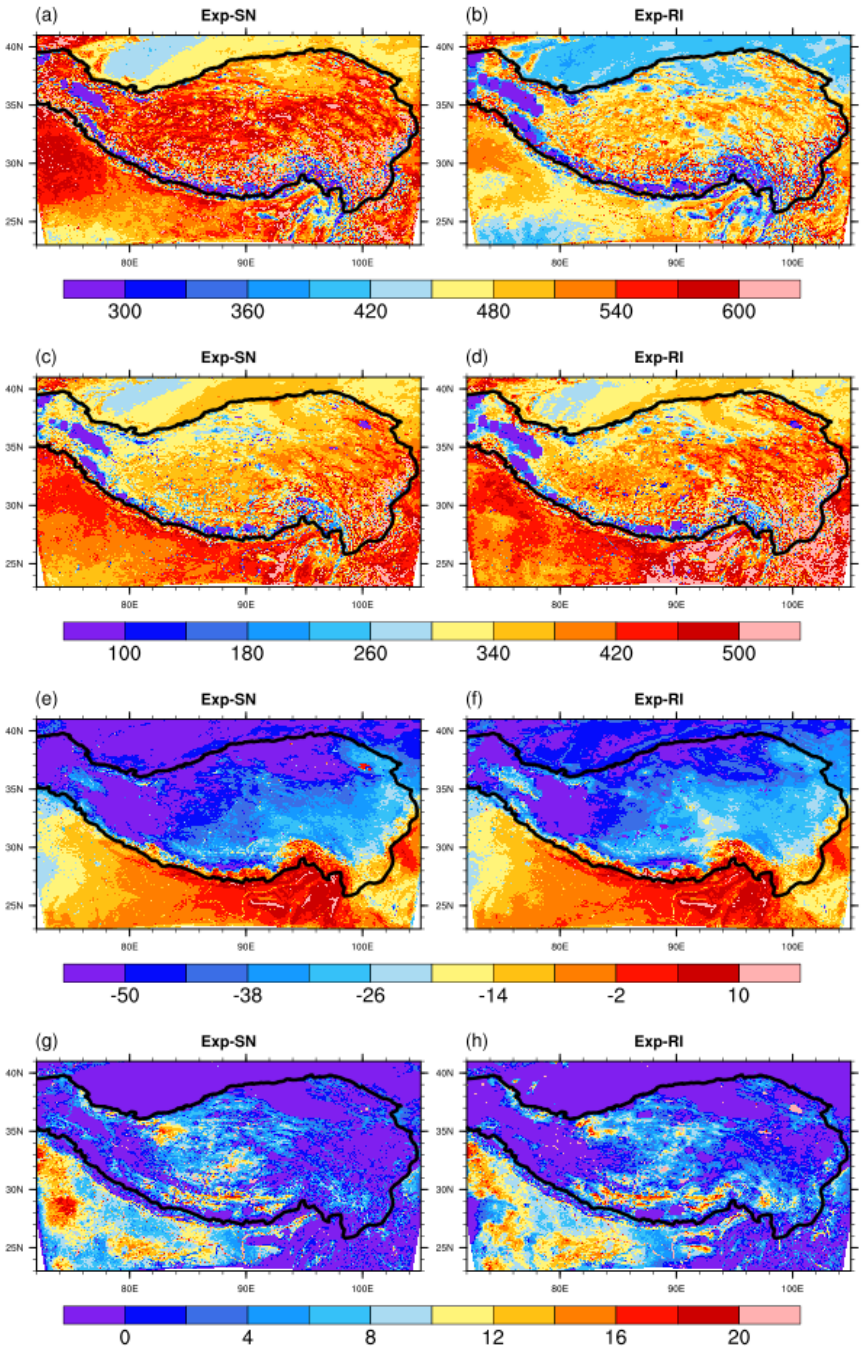

Figure 14

3-yr averaged surface net radiation, and the sum of sensible heat and latent heat fluxes at 06:00 (Exp-SN: a, c; Exp-RI: b, d) and 18:00 UTC (Exp-SN: e, g; Exp-RI: f, h). Units: W/m2. Note: The designations employed and the presentation of the material on this map do not imply the expression of any opinion whatsoever on the part of Research Square concerning the legal status of any country, territory, city or area or of its authorities, or concerning the delimitation of its frontiers or boundaries. This map has been provided by the authors.

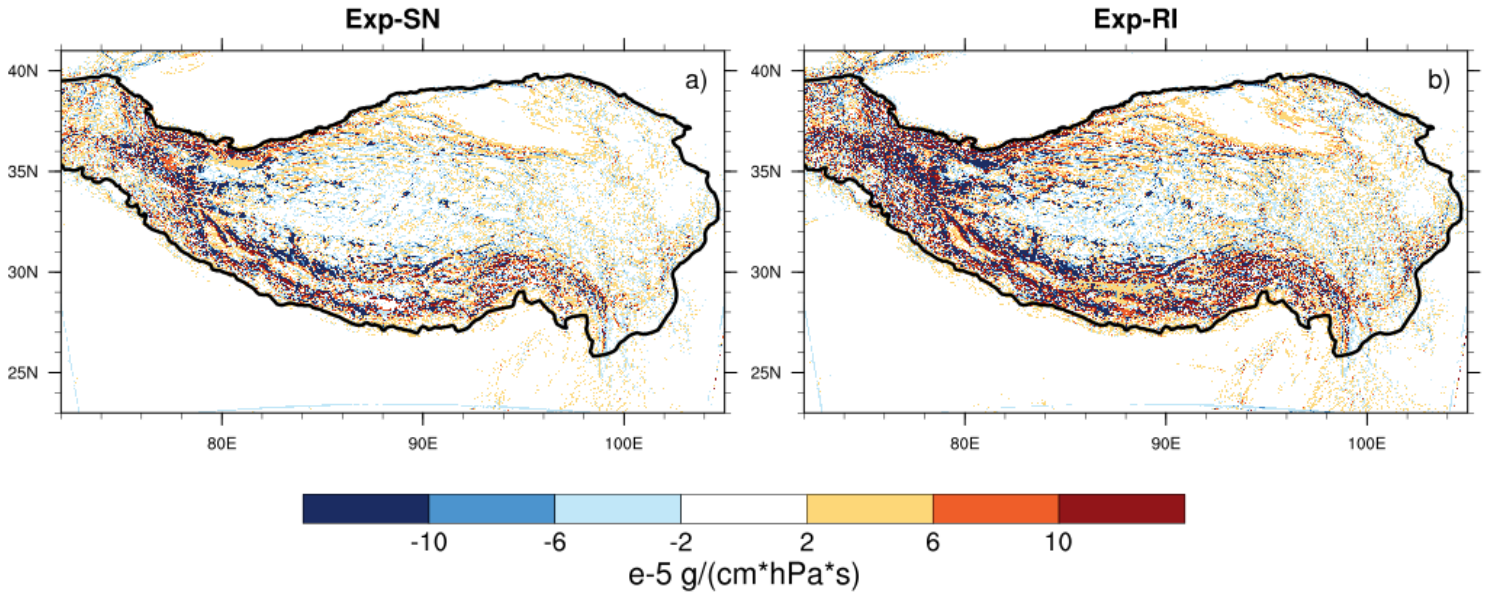

Figure 15

3-yr averaged moisture flux divergence at low level (500hPa) over the TP in the WRF experiments. Note: The designations employed and the presentation of the material on this map do not imply the expression of any opinion whatsoever on the part of Research Square concerning the legal status of any country, territory, city or area or of its authorities, or concerning the delimitation of its frontiers or boundaries. This map has been provided by the authors.